Real-Time Near-Field mmWave Measurements Using Screen-Printed Metasurfaces and IR Camera

Lundgren, Johan; Martin, Torleif; Khalid, Hamza ; Zabihipour, Marzieh ; Tu, Deyu; Engquist, Isak ; Sjöberg, Daniel; Gustafsson, Mats

2024

CODEN:LUTEDX/(TEAT-7282)/1-26/(2024)

Real-Time Near-Field mmWave Measurements Using Screen-Printed Metasurfaces and IR Camera

Johan Lundgren, Torleif Martin, Hamza Khalid, Marzieh Zabihipour, Deyu Tu, Isak Engquist, Daniel Sjöberg, Mats Gustafsson

Electromagnetic Theory
Department of Electrical and Information Technology
Lund University
Sweden

(TEAT-7282)/1-26/(2024): J. Lundgren, *et al.*, Real-Time Near-Field mmWave Measurements

Johan Lundgren, Daniel Sjöberg, Mats Gustafsson
{johan.lundgren, daniel.sjoberg,mats.gustafsson}@eit.lth.se

Department of Electrical and Information Technology
Electromagnetic Theory
Lund University
P.O. Box 118
SE-221 00 Lund
Sweden

Torleif Martin
{torleif.martin@qamcom.se}

Qamcom Research & Technology,
Linköping,
Sweden

Hamza Khalid, Marzieh Zabihipour, Deyu Tu, Isak Engquist
{hamza.khalid, marzieh.zabihipour, deyu.tu, isak.engquist}@liu.se

Linköping University,
Norrköping,
Sweden

This is an author produced preprint version as part of a technical report series from the Electromagnetic Theory group at Lund University, Sweden. Homepage `https://www.eit.lth.se` and `https://portal.research.lu.se`.

Editor: Mats Gustafsson

Abstract

This paper elaborates on a technique for rapid real-time imaging of millimeter wave (mmWave) power density over surfaces of several wavelengths in size. The approach involves utilizing a screen-printed metasurface equipped with elements designed for absorption of mmWaves, along with an infrared camera to monitor temperature changes due to the absorption. By modulating the transmitted signal and applying the metasurface technique, which concentrates absorbed power onto specific regions, we successfully detected typical mmWave power levels. This method provides an efficient, non-contact means of rapidly evaluating and characterizing devices emitting in the mmWave spectrum. To illustrate the efficacy of the technique, we present two case studies at 28 GHz: fault detection on a 256 element square array antenna in the Ka-band, and mmWave power density imaging in the near-field of a mobile phone mockup over surfaces measuring 58 square centimeters (51 square wavelengths at 28 GHz). The results obtained can be analyzed in both the time and frequency domains, augmenting comprehension and assessment capabilities.

1 Introduction

As 5G and forthcoming generations expand, the adoption of millimeter-wave (mmWave) devices is on the rise [3, 15]. This trend is accompanied by the utilization of electrically large radiating structures, such as phased arrays, to facilitate advanced beamforming techniques [13, 18, 21]. The technology is experiencing heightened demands across various sectors, including 5G, satellite communication, and radar applications [3, 18, 21]. Modern manufacturing processes of these systems enable the seamless integration of array elements with electronic control systems on printed circuit boards (PCBs) [21]. However, different applications exhibit diverse key metrics. For instance, in handheld devices, the focus may primarily be on radiated and near-field power. On the other hand, larger structures prioritize factors like radiation pattern, polarization and tapering control. Therefore, the precise control of element phase and amplitude assumes paramount importance in catering to these varying application requirements.

Due to integration complexities, identifying manufacturing or programming errors on the production line or those arising from extended usage can pose challenges. Traditional radiation pattern measurements struggle to pinpoint deviations in performance down to specific elements or components within the array antenna. While techniques exist to address this issue see *e.g.*, [8, 12, 23, 24], this paper presents an alternative approach to measuring field amplitude based on detection of infrared (IR) radiation resulting from the heating of a metasurface in front of a transmitting device. The temperature evolution of these metasurface elements, spaced approximately $\lambda/2$ apart, excels in detecting, comparably, weaker signals, as the absorbed power is localized to specific regions on a surface with otherwise limited heat dissipation capabilities [19]. The imaged metasurface serves as an indirect indicator of the mmWave power density at its position through the interaction of the electric field and the metasurface. The technique has previously been demonstrated for

12 GHz with data processed in the time domain imaging few (1–9) elements simultaneously [19]. Similar approaches exist for other frequencies [9, 16, 17], high power densities [2, 5, 26] with polarization information [7], or with the use of homogeneous sheets [11, 25] combined with a fluorescent layer to circumvent the use of an IR camera over a CMOS camera [10].

In this paper, we present a metasurface design consisting of approximately 200 elements, enabling rapid measurement of the radiated field over a surface area of approximately $10 \times 10\,\mathrm{cm}^2$. This surface can be positioned directly above an antenna structure to image the near field. Screen printing is utilized as a cost-effective method for constructing the metasurface. On/off signal modulation, combined with localized heating of the metasurface elements, is used to enable differential measurements, exploiting the high sensitivity of the IR camera. Image processing automatically determines the regions for localized heating and the boundary regions between the elements in the live camera video feed and enables simultaneous real-time processing of the data for electrically large surfaces. Effects of IR camera resolution, modulation frequency, and temperature drift are also discussed.

This paper showcases the first practical application of the technique and post-processing routines for modern communication technologies in two main areas:

1. Amplitude fault detection of a 'RESA-S Ka', prototype [28], a fully integrated phased array flat panel antenna terminal specifically crafted for Satcom 'On-The-Move' applications spanning LEO/MEO/GEO constellations.

2. Amplitude near-field measurements of a mobile phone mock-up from measurements of a laterally translated metasurface providing a densely sampled image.

2 Physical model and thermal focus

The measurement technique relies on the absorption of incoming electromagnetic waves within the mmWave spectrum, facilitated by a metasurface [19]. In this section, we introduce the metrics that can be extracted from a single element of this metasurface, and relate them to their physical origin.

2.1 Measurement setup

The metasurface in this work consists of numerous metasurface elements tuned to dissipate energy from an impinging linearly polarized wave through Ohmic losses induced by currents, see Fig. 1. Thus, for circular/elliptical polarization one linear component is registered and the other component is ideally completely transmitted. In Fig. 1, the measurement setup is illustrated for a metasurface with approximately 2000 elements positioned at a plane of interest away from a radiating device and a distance, d, from an IR camera. In this work, the camera is positioned directly in front of the antenna. This placement can cause reflections that may interfere, depending on the power level and radiation pattern of the radiating device, as well

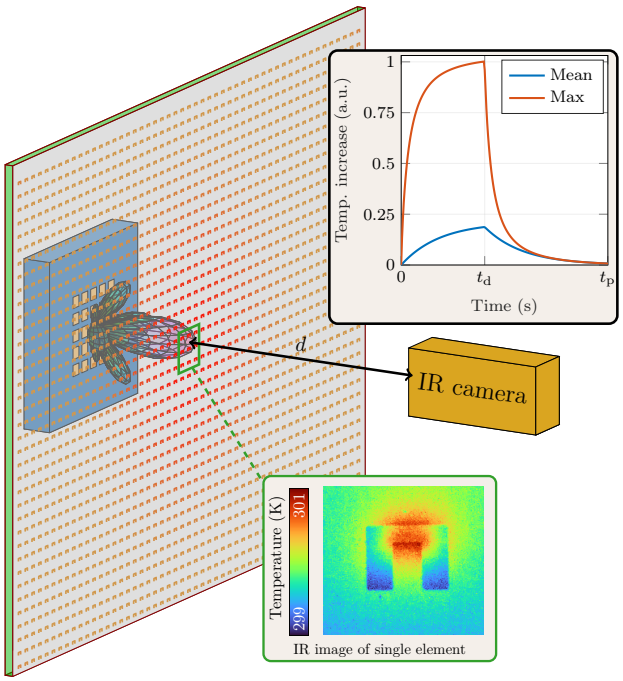

Figure 1: Schematic diagram of the measurement setup: A radiating object is positioned behind a metasurface composed of numerous elements, which is placed at a distance, d, from an infrared camera. The inset shows the measured data for a single element, with the accompanying graph depicting the simulated mean and maximum temperatures in the specified region, based on an excitation described by (2.2).

as the distance to the antenna. To avoid these issues, the camera can for instance be positioned off-center, or with an additional frequency selective surface introduced between the metasurface and the IR camera.

The inset image of Fig. 1 displays a measured metasurface pixel (unit cell) cropped from a single frame of an IR video feed in which the Ohmic losses generate heat. Consequently, the generated heat diffuses across the surface through conduction, interacts with the surrounding air via convection, and releases energy through radiation [14]. An IR camera captures and maps the heat from the metasurface elements through the captured IR photons to the squared amplitude of the electric field, aligned with the polarization dictated by the elements. Through normalization this quantity is further mentioned as the power density for a given polarization. The design and performance is further discussed in section 4 of the paper.

2.2 Methodologies

The process of absorbing incoming electromagnetic radiation and converting it into heat is a multiphysical process. The subsequent heat diffusion over a surface, in this case the metasurface, follows the thermal-diffusion equation [14]. Spatial details of an electric field distribution over this surface can be challenging due to heat diffusion spreading thermal energy. This results in an undesirable reduction in signal-to-noise

ratio (SNR) in the detected IR photons at each imaged point as well as an increase in correlation to neighboring regions on the diffusion surface.

One well-established methodology is lock-in thermography [10, 31] with numerous other techniques presented across various IR non-destructive testing contexts [6]. In lock-in thermography, a periodically modulated source signal is used to heat a structure, allowing for measurements over several periods and thus an effective suppression of noise. Further, introducing modulation to the heating source, *i.e.*, in this work the input signal to the radiating mmWave device, allows us to influence the spread of thermal energy, as indicated by the thermal diffusion length, denoted as D [2]

$$D = \sqrt{\frac{\alpha}{\pi f}} \tag{2.1}$$

where α is the material-dependent thermal diffusivity of the absorbing surface or slab, and f is the frequency of the modulation, in this work set to 0.2 Hz. The modulation can take many forms and we consider a simple modulation of a rectangular on/off pulse of length $t_\mathrm{p} = 5\,\mathrm{s}$ transmitting for $t_\mathrm{e} = 2\,\mathrm{s}$ (on). Hence, for a single period the absorbed power, P, in a part of the element is

$$P(t) = \begin{cases} P_0, & 0 < t < t_\mathrm{e} \\ 0, & t_\mathrm{e} < t < t_\mathrm{p} \end{cases} \tag{2.2}$$

Using this modulation, consistently employed throughout the paper, we can express an approximate solution for the heat equation in the case of a thin homogeneous sheet for a single period as

$$u(t) = \begin{cases} \Delta u(1 - \mathrm{e}^{-t/\tau_\mathrm{r}}) + u_\mathrm{o}, & 0 < t < t_\mathrm{e} \\ \Delta u(1 - \mathrm{e}^{-t_\mathrm{e}/\tau_\mathrm{r}})\mathrm{e}^{-(t-t_\mathrm{e})/\tau_\mathrm{d}} + u_\mathrm{o}, & t_\mathrm{e} < t < t_\mathrm{p} \end{cases} \tag{2.3}$$

where u is the temperature and the parameters, Δu, τ_r, τ_d, and u_o are the strength, rise and decay time constants, and temperature offset respectively, see Fig. 1. They are dependent upon the selected materials—through specific heat capacity, thermal conductivity, and emissivity [14]—the region of interest, and the sheet's geometry—taking into account its non-uniform composition—and lastly the frequency of the incident wave. Further analysis of this simple model can be extended to explicitly include additional parameters.

Experimental data are expected to exhibit similar trends and can be effectively fitted to (2.3). In this context, we observe that the signal generally behaves in a periodic manner (*i.e.*, $u(0) = u(t_\mathrm{p})$).

In a noiseless setting, this periodicity is not achieved until after a few periods due to the gradual heating of the object. Factors such as t_d, input power, and material properties influence this behavior. Measurements are conducted over several periods and then combined to mitigate unwanted effects like thermal noise and temperature drifts. However, complete removal of these effects is not realistic. Noise and environmental changes, such as temperature fluctuations over time, impact the system and consequently the periodic behavior $u(0) = u(t_\mathrm{p})$.

This periodicity is nonetheless important, as the temperature difference during a period provides information on the absorbed energy. With no preference between $t = 0$ and $t = t_\mathrm{p}$ the measured temperature difference (also referred to as the signal) is therefore calculated as the average of $u(t_\mathrm{d}) - u(0)$ and $u(t_\mathrm{d}) - u(t_\mathrm{p})$ as

$$\Delta T = u(t_\mathrm{d}) - \frac{u(0) + u(t_\mathrm{p})}{2} \tag{2.4}$$

The impact of (2.4) is not apparent in the simulated signal of Fig. 1 as $u(0) \approx u(t_\mathrm{p})$ but is noticeable for measured data with significantly lower SNR.

2.3 Metasurface thermal focus and IR image

In addition to modulating the input to limit diffusion and enhance the SNR through repetition, we can improve these qualities further by optimizing the design of the absorbing structure [19]. In this work, we achieve this by localizing the heat generation to smaller regions of the surface. This will secondarily affect the IR image of the metasurface as the heated region should be resolved.

The metasurface consists of several materials and is subject to minor temperature increases, making (2.3) an approximate solution. Consequently, the rise and decay time constants, τ_r and τ_d, depend on both material properties and geometry, yet remain effectively independent of the exciting waves. The general shape of the output signal (2.3) represents a noise-free setting. A depiction of simulated (using COMSOL Multiphysics) absorbed mmWave energy and resulting heat generation, as per (2.2) and (2.3), is illustrated in the graph in Fig. 1. The figure illustrates a single simulated metasurface pixel of the design, with geometry and further details provided in Sec. 4, showing the temporal evolution of the spatial maximal and mean temperatures over a metasurface element. Both temperature curves follow (2.3), albeit with different parameter values.

In a measurement scenario, the maximal temperature offers a higher SNR than the mean temperature, where each pixel in the IR camera would have the same, but lower, SNR. The metasurface design localizes heating to the central part of the element, resulting in a higher maximal temperature compared to the mean temperature. A design with further localized losses such as a surface-mounted resistor on an otherwise highly conductive metasurface element can experience a higher maximal temperature compared to the mean than the design in this work [19].

Establishing a thermal focus through electromagnetic design results in a signal with a higher SNR compared to a scenario without such a focus. However, when conducting measurements, the characteristics of the IR camera must be taken into account. Specifically, the camera used in this study is a FLIR A655sc with a resolution of 640×480 pixels. These pixels capture the image of our metasurface, and we are limited by this resolution.

Fig. 2 shows a measurement of the absolute temperature at time $t = t_\mathrm{e}$. An image of a single element, when approximately 10 metasurface elements are in view, is displayed, revealing the detailed structure and the localization of heat generation. If the same camera views 200 or 2000 metasurface elements, the resulting image

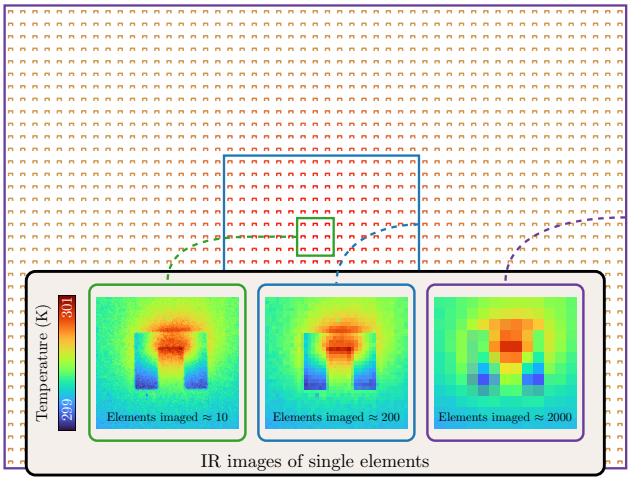

Figure 2: Illustration of a single element image when using an IR camera of 640×480 pixels having approximately 10, 200 or 2000 elements in field of view.

will have a lower resolution, as shown in the additional images. When viewing the lowest resolution image, where 2000 elements are in view, the result is coarse. While one element might be visible, another might be misaligned with the IR pixels, resulting in varying image quality. Therefore, it is important to have as many pixels as possible to ensure consistent imaging quality across the entire surface. These images in the figure are created by downsampling the original image rather than from new measurements to have a comparison of only the resolution and not other measurement setup-related connections.

In general, a measurement point with an IR camera should cover a minimum of 3×3 pixels [27]. An element and thermal focus smaller than or similar in size to this will not gain any benefit other than reduced convective losses. Therefore, when setting up measurements, the area of interest should be chosen such that the camera can capture the metasurface elements at the highest possible resolution. This can be achieved by adjusting the distance, d, in Fig. 1, or by using various lenses. The measurement quality will also depend on whether the distance or a lens is used, with increased distance adding more air and turbulence, which can affect the results.

3 Measurement processing

3.1 Camera and region of interest

When implementing the technique outlined in this paper we deployed an infrared camera with a metasurface (aligned with the xy-plane) at a specified distance, d, in the z-direction, where the measurement of the electromagnetic wave is carried out. The camera is equipped with a finite number of pixels, and captures images over a defined duration, typically encompassing several modulation periods, t_p. As previously mentioned a bolometric uncooled IR camera (FLIR A655sc) with a resolution of 640 × 480 pixels is used. The camera has an accuracy of ±2 K for the cap-

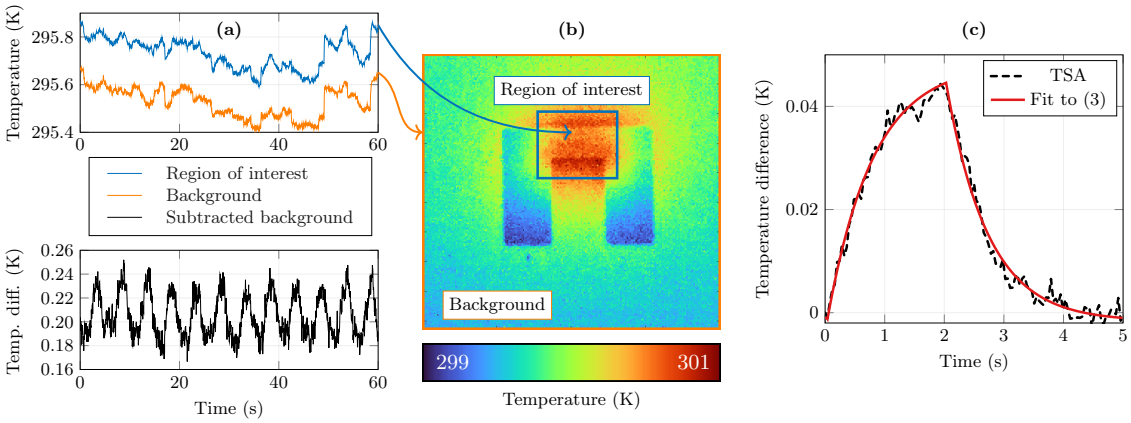

Figure 3: Demonstration of the measurement processing. In column (a) a measured temperature evolution of the mean temperature in the region of interest (blue) and the background temperature (orange). The temperature difference between them is shown in black. In column (b) the IR image from a typical measurement is shown, and not related to the data set in columns (a) and (c), where the region of interest is within the blue border and the background is the orange border. The time synchronous average (TSA) temperature difference is shown in black in column (c) where the red line displays a fit to the expression in (2.3).

tured temperature interval and a noise equivalent temperature difference (NETD) of 30 mK. Hence, the camera is good at measuring temperature differences ΔT across the image, but less good at measuring the absolute temperature.

Another advantage of localized heat generation, besides the aforementioned SNR improvement and reduction of the thermal diffusion, is its positive impact on calibrating the temporal evolution of background temperature. Measured signals over several periods rarely display the clarity shown in Figure 1 unless the signal is sufficiently strong ($\Delta T > 0.5\,\mathrm{K}$). External factors can introduce both long- and short-term fluctuations in the observed temperature, complicating signal detection. However, with localized heated regions, several non-heated areas on the surface naturally serve as localized reference temperatures. These references effectively eliminate unwanted effects, as discussed further in Section 3.1.

When observing the temperature changes on the metasurface, the camera is susceptible to various sources of interference, such as thermal noise, gradual environmental heating, background temperature, heating of camera pixels, and air turbulence between the camera and the metasurface.

The maximal temperature in Fig. 1 presents an idealized representation of a noise-free measurement of the warmest point. In an actual measurement scenario, the simulated peak temperature is replaced by a region of interest of minimally 9 pixels [27]. This region of interest is chosen to be constant in time and is automatically detected for every element using image processing. All elements on the metasurface will have an identical size of region of interest and placement. A well-resolved image of the metasurface elements then helps with the alignment of the

IR pixels over the metasurface element for consistent measurements. An example of the region of interest is illustrated by the blue border in Fig. 3 (b), emphasizing the predominant heating area. The size of the region can be estimated based on the thermal diffusion in the substrate but it is also connected to the thermal parameters of the element and their emissivity as well as the geometry of the design and signal modulation (2.1). The consequence of altering the region size between measurements is primarily that the detected signal strength in the region of interest will change, presenting a calibration change in converting the temperature to EM power.

Consider a measurement process conducted over a metasurface, where each image captured by the infrared camera consists of $n \times m$ metasurface elements with a region of interest as displayed in Fig. 3 (b). The measured mean temperature in the region of interest over 60 seconds for a single metasurface illuminated by a 28 GHz signal modulated according to to (2.2), for 12 periods, is displayed in the blue line in Fig. 3 (a). This data set is not taken from the image but from a separate measurement conducted at lower power levels to illustrate key points.

The expected periodic signal is not immediately discernible and appears to be dominated by other effects. This complexity arises because the measurement scenario is more intricate than depicted in the simulated Fig. 1, as the photons must be detected by the IR camera. The emissivity of different materials affects the temperature changes observed on the metasurface, and the IR camera is susceptible to various sources of interference, such as thermal noise, gradual environmental heating, background temperature, heating of camera pixels, and air turbulence between the camera and the metasurface. These effects may not necessarily extend uniformly across the entire measurement region, leading to fluctuations over time and between measurement points on the surface.

However, by introducing a thermal focus, we also create regions within a metasurface element that remain unaffected by the element's heating. These regions serve as localized backgrounds, allowing for compensation of many undesired effects unrelated to the measurement.

The background region for each metasurface pixel is defined as the edge pixels of each respective IR camera image, as illustrated for a single metasurface pixel by the IR pixels underneath the orange line in Fig. 3 (b). This background data is displayed over time in the orange line of Fig. 3 (a). Both curves exhibit a similar overall shape, but subtracting one from the other reveals the emergence of a periodic signal, as shown by the black line in Fig. 3 (a).

In this work identification of the elements was done from a reference measurement in which a strong signal was used to illuminate the metasurface or a warm object was placed behind effectively displaying a shadow image of the elements in the camera image as some of the manufactured metasurface designs were made of PET (partly transparent to visible and IR).

The relative temperature of the region of interest, compared to the background, is monitored over multiple periods for all elements. The subsequent time-domain processing includes computing the time synchronous average (TSA) [4], utilizing the predefined period time t_{p}.

In Fig. 3 (c) the example measurement over a single metasurface element is displayed using time-domain processing [19]. The TSA signal is displayed in the dashed black line with a shape resembling (2.3). The fitting of this data to (2.3) is illustrated in the red curve of Fig. 3 (c). The model described in (2.3) is valid under the condition that $\Delta u \ll u$. In this regime, the time constants remain independent of the strength of the exciting signal and should not change between measurements. One approach to determine these constants for each metasurface element is to illuminate the metasurface with a strong incident field, enabling their precise measurement with a high SNR. These constants can then be applied consistently, even in scenarios with lower SNR. However, in this study, the time constants were treated as free parameters for each metasurface pixel in each measurement and were fitted alongside the other parameters of equation (2.3).

3.2 Measured number of periods

A practical approach to noise suppression involves measuring multiple periods, but determining the optimal number of periods remains a crucial consideration. To demonstrate how the measured signal converges with an increasing number of periods, it is generally assumed that more periods yield better accuracy. In this study, we arbitrarily measure 23 periods to represent the most accurate value, comparing the signal's consistency when fewer periods are used from the same dataset. Figure 4 illustrates the relative difference in the measured signal over several periods compared to the results obtained after $N = 23$ periods, defined as

$$\delta_n = \frac{|\Delta T_n - \Delta T_N|}{\Delta T_N} \tag{3.1}$$

where n is the measured number of periods.

The measured device is an open-ended waveguide probe operating at 28 GHz with a distance of 5 mm to the metasurface (displayed in inset of Fig. 12). During the measurement, 204 metasurface elements were simultaneously measured with an IR camera framerate of 25 Hz.

Figure 4 emphasizes the relationship between the number of measured periods and the impact of thermal noise. For signals ranging from $1-10\,\mathrm{mW/cm^2}$, averaging $2-5$ periods provide a value within $\approx 5\%$ of the significantly longer measurement time. However, at lower power densities, the signal exhibits instability even with 23 periods, necessitating more measurements. Throughout the remainder of this work, 12 periods are utilized unless otherwise specified.

3.3 Frequency domain data

Another method for extracting information from the measurement involves using complex frequency domain data [22]. Specifically, the low-frequency component can be utilized to assess the background temperature content, while the high-frequency component of the pixels near the edges of the element are stronger and thus help identifying the elements. In Fig. 5, the frequency domain data for a measurement

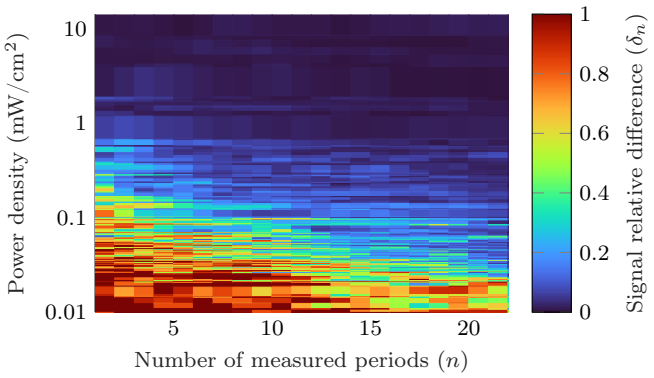

Figure 4: The relative difference (3.1) of the measured signal from 204 metasurface elements for various power densities as a function of the number of measured periods.

(the measurement displayed in Fig. 3 (b)) of a single metasurface pixel is presented within the $0.1 - 0.9\,\mathrm{Hz}$ range. The signal with a 5 s period prominently exhibits a significant peak at 0.2 Hz, further illustrated in the inset image displaying the frequency domain content at 0.2 Hz. Utilizing the frequency domain and the signal's periodicity offers an alternative and rapid method for acquiring images of radiating fields. Other modulation techniques can potentially enhance the sinusoidal nature of the output signal.

In comparison to time-domain processing, the frequency-based approach enables us to obtain an image for processing without requiring background subtraction or the specification of a particular region of interest. While this method ensures rapid measurements and processing due to minimal computation, it lacks the capacity to eliminate undesired effects contained within the modulation frequency and, generally, as a result, may not achieve the same dynamic range as the preceding time-domain processing technique.

Significantly, both time and frequency processing can synergize and complement each other when used together. For example, visualizing images of the frequency domain at the modulation frequency can provide valuable data, assisting in the automatic detection of the region of interest for subsequent time-domain processing. Alternatively, normalized frequency domain data can be employed as pixel-by-pixel weights in the time domain, offering a measurement-independent approach for defining the region of interest, where the user can specify the size and placement.

In a measurement involving $n \times m$ metasurface pixels, each metasurface pixel produces a single measurement point. In the designed metasurfaces, the distance between elements is approximately $\lambda/2$ (at 28 GHz), determining the sampling of the final image for a single measurement. To achieve a higher sampling, multiple measurements can be combined by introducing a sub-$\lambda/2$ offset. This process can be applied to the final time-domain processed results of a matrix with $n \times m$ elements or frequency domain data, depending on the pixel size of the utilized camera. Both types of results are presented in Sec. 6.

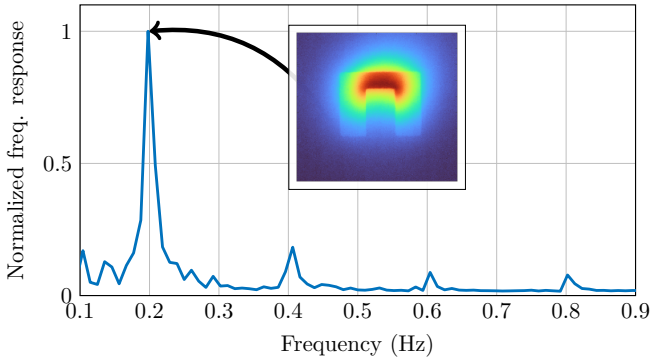

Figure 5: The frequency content of thermal data for the measurement presented in Fig. 3 (b). The inset image shows the frame for the 0.2 Hz content.

4 Design and manufacturing

4.1 Initial considerations

The metasurface demonstrated in this work was designed to operate for 28 GHz but can operate in the range of $24 - 32$ GHz, see Fig. 6. In contrast to prior approaches where a resistor was soldered onto each element [19], this work explored employing a single material for the entire element, utilizing screen printing technology [29, 34]. The motivation for the manufacturing approach of resistive elements was a result of several factors such as high resolution, cost-effective, low waste, high output, and ease of manufacturing [1, 32, 35]. Previous work has shown that arrays with several hundred identical elements can be reliably produced using screen printing [33]. The resulting sheet resistance of the printed ink mixtures ranged between around 3-42 Ω/□. This range of sheet resistances affects design decisions, as achieving the desired electromagnetic properties depends on the resistance values and consequently the number of squares. Further, in screen printing, there is a minimum dimension requirement of 0.5 mm that must be maintained for manufacturing consistency.

Thermal considerations focused on selecting a material with high emissivity, low thermal conductivity, and specific heat capacity [19]. In the design, the substrate housing the resistive elements was made of PET (Polyethylene terephthalate, *Polifoil Bias* purchased from Policrom Screen). PET is a transparent polymer with relatively low thermal conductivity, typically ranging from 0.15 to 0.25 W / (m K) [30, p. 2794]. The thickness of the PET (50 / 125 µm) directly influences the received signal, with a thicker substrate having more mass to effectively heat. The resistive elements comprise a blend of carbon and silver to achieve the desired resistivity values.

4.2 Simulations

The complete metasurface structure underwent simulation in COMSOL Multiphysics, including both electromagnetic and thermal effects. Electromagnetically the design was also simulated in CST (non-thermal part), where the design was optimized to maximize absorbed power while having a reflected power of less than 1/4 of the

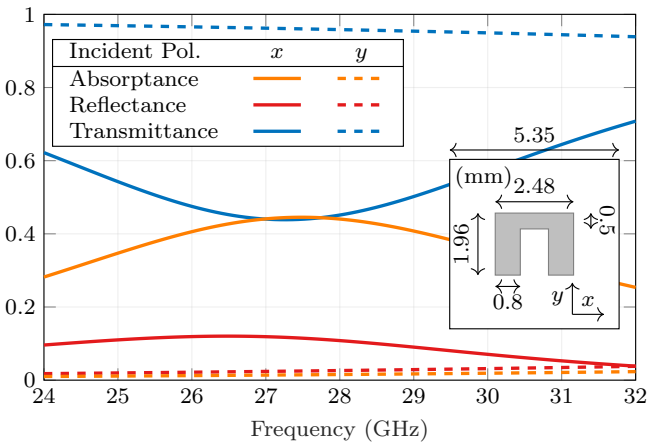

Figure 6: Simulated (CST) absorbed, reflected, and transmitted power for two incident polarizations: x (solid) and y (dashed). The metasurface element design shown in the inset is placed on a 50 µm thick PET substrate with a relative permittivity of $\varepsilon_r = 3.1$.

absorbed power —a deliberate trade-off chosen between absorption and interaction with the measurement object through reflections. The design features a linearly polarized dipole array with a geometrically straightforward structure, adhering to manufacturing constraints on parameters like width and thickness.

Figure 6 illustrates the geometry of a single metasurface pixel and its frequency response as simulated through CST, utilizing periodic boundary conditions. The element is modeled as a surface impedance with a sheet resistance of 7.3 Ω/□, positioned on a PET substrate with a thickness of 50 µm and a simulated relative permittivity of $\varepsilon_r = 3.1$. The absorption and reflection rates from co-polarized illumination at 28 GHz are 44% and 11%, respectively, with similar values for cross-polarization at 1.5% and 2.5%.

The metasurface element shown in Fig. 6 occupies 12% of the total area. When imaging 200 elements using a 640 × 480 pixel IR camera, this configuration results in ≈ 1500 IR camera pixels per metasurface pixel and ≈ 180 IR camera pixels per metasurface element, resulting in images as illustrated in Fig. 2.

4.3 Manufacturing

The fabrication of the metasurface utilized screen printing technology which involves depositing layers of inks onto the substrate using a screen mask. The design of this screen mask can be tailored to specific requirements, comprising a mesh of varying sizes that permits ink to pass through only in designated regions while blocking it in others. To fabricate the desired metasurface, the substrate was cleaned with isopropanol and preheated at 120°C for 20 minutes in an oven to remove any moisture present. After this, the screen mask was placed on top of the substrate and the ink was deposited on top of the mask, along one of its edges. A squeegee was used to push the ink forward along the mask, and simultaneously down through the openings

Table 1: Manufactured metasurfaces, ink composition, substrate material, thicknesses, and sheet resistance of the elements.

Ink composition by weight (Ag/C)	Substrate material	Thickness (μm)	Element sheet resistance (Ω/□)
51/49 - stored	Paper	250	35 ± 7
55/45	PET	125	3 ± 0.5
51/49	PET	125	6 ± 1
51/49 - stored	PET	125	35 ± 7
51/49 - stored	PET	50	35 ± 7
51/49 - stored	PET	50	35 ± 7

in the mask onto the substrate, leaving behind the required printed structures. The printed substrate was then again heated at 120°C for around 5 minutes to evaporate the solvents present within the ink. The screen printing was performed on a semi-automated screen printer EKRA E2 using a screen printing mesh of mesh count 140, using a mixture of carbon (DuPont 7102) and silver (DuPont 5028) inks on three different substrates: 50/125 μm thick PET substrates and 250 μm thick paper substrate (Albato). Three different sheet resistance values were achieved using three different silver-carbon ink mixtures: freshly made 55-45 Ag-C, freshly made 51-49 Ag-C, and 51-49 Ag-C stored for 3 months. For each composition, five samples were taken out of the printed metasurface and measured to determine sheet resistance with respective tolerance. Metasurfaces for both single and dual polarization were created by interspacing a design translated and rotated 90 degrees in the plane. Focusing on the single polarized designs in this work, one printed on PET is depicted in Fig. 7, along with a close-up view of a single metasurface element. Altogether, six distinct sheets were produced, as specified and identified in Table 1. Two of the sheets have identical parameters, 50 μm thick PET and a sheet resistance of $35 \pm 7\,\Omega/\square$. Two sheets were manufactured to verify production quality.

5 Results for printed metasurfaces

The metasurfaces produced, as detailed in Sec. 4, were employed in a series of measurements in which the modulation is described by (2.2). The measurements were conducted across various scenarios with differing areas of interest, resulting in a variable number of observed metasurface pixels. Specifically, the range of the images during our measurements included 180 to 204 metasurface elements, corresponding to an imaged area of $50 - 60\,\mathrm{cm}^2$. This demonstrates the technique's capability for robust and comprehensive data collection, supporting large-scale simultaneous electrical area imaging under various experimental conditions.

5.1 Performance testing

To evaluate the responsiveness, indicated by the time constants τ_r and τ_d in (2.3), and the total signal strength of the metasurfaces produced with various substrate materials, thicknesses, and sheet resistance (as presented in Table. 1), measurements

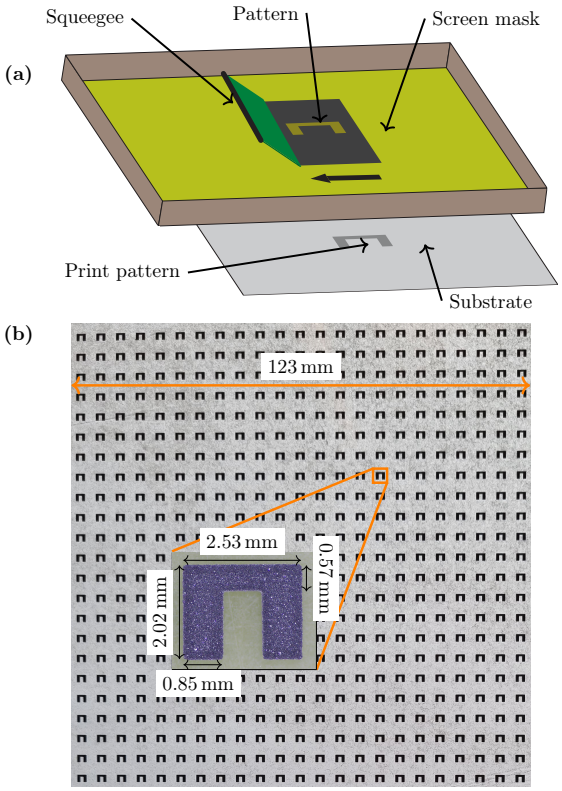

Figure 7: a) Screen printing illustration. b) Photograph of a manufactured metasurface printed on PET with an element highlighted with dimensions.

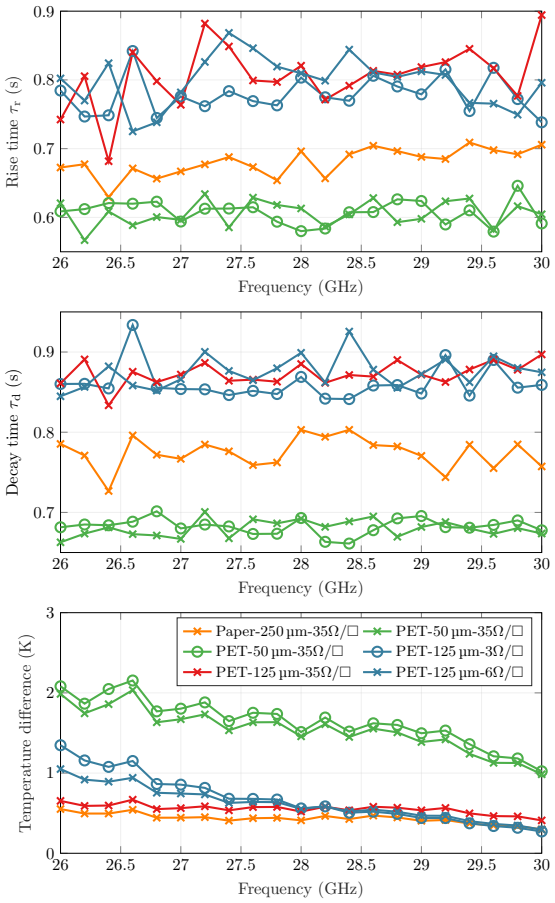

Figure 8: Fitted values, to (2.3), of the rise τ_{r} (top) and decay τ_{d} (middle) time constant from (2.3) along with the measurement signal output (bottom) for the manufactured metasurfaces in Tab. 1.

were conducted using a standard gain horn antenna (MVG SGH2650-42). It was operating at a fixed output power of 10 mW (10 dBm) illuminated the manufactured metasurfaces at a distance of 5 mm. The time-domain processing routine detailed in Sec. 3.1, involving the fitting of all parameters in equation (2.3), was consistently applied with identical settings of the region of interest, measurement time *etc.* across all measurements. In Fig. 8 the comprehensive output, ΔT, along with the rise and decay time constants (τ_r, τ_d), is presented.

As detailed in Sec. 2, the rise and decay rates of the average temperature within a region of interest are directly linked to the thermal properties of the metasurface and are influenced by the absorbed power, rendering them independent of frequency. By comparing the two identically manufactured samples (green), we observe a slight spread of the data that remains relatively stable across the displayed frequency interval.

Table 1 demonstrates the ink mixtures varied across the prints. Consequently, while the mass density and specific heat capacity of the metasurface element may undergo minor variations, the substrate comprises the bulk of the mass and should not have a significant effect. Additionally, within the considered conductivity ranges, variations subtly adjust thermal conductivity—a secondary effect. The time constants do not exhibit dependency on the resistivity of the elements.

Furthermore, it is anticipated that there may be slight differences in both the rise time and decay time. As the rise time tends to be faster, in general, the modulation pulse is selected to have a duty cycle of less than 50 %, *i.e.*, $t_\mathrm{e} \leq t_\mathrm{p}/2$.

The primary difference between the detected temperature increase lies within the thickness and material of the substrate. These factors influence the design by affecting both the frequency performance, by shifting the response, and the mass and consequently energy required for heating. Notably, despite the paper-based metasurface being twice as thick as the thicker PET substrate, their performances (as seen in the bottom row of Fig. 8) are comparable. This is due to differences in mass density and thermal conductivity between the two materials.

We note that the variation in frequency behavior largely arises from differences in sheet resistance values. This impact of sheet resistance is evident when comparing the slope of the temperature increase in the blue and red curves, where the only variable is sheet resistance. This difference directly influences the performance of the design. Specifically, additional simulations of the design in Fig. 6 show that it absorbs less co-polarized and more cross-polarized incident signals as the resistance values increase. Lower resistance values result in a narrower bandwidth with a steeper slope. Furthermore, the total temperature increase in Fig. 8 deviates from the expected outcome observed from the absorptance in Fig. 6, in part attributable to material parameters beyond the scope of simulations and challenges in achieving precise resistance values.

Considering the measurement perspective, among the available metasurfaces, the 50 µm PET with $35 \pm 7\,\Omega/\square$ exhibits the quickest response and highest signal output, making it the preferred choice for this measurement and subsequent ones. The resistance differed from the initial design in Fig. 6 and a simulated absorptance at 28 GHz for this design is 20% with a 2.4% reflectance.

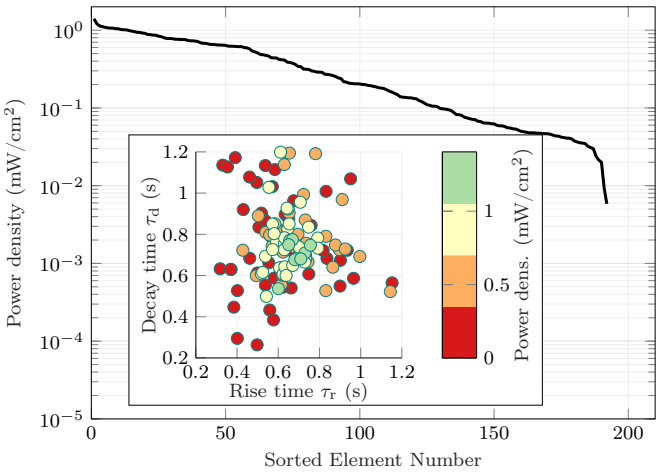

Figure 9: Distribution of measured power density for 204 metasurface pixels and their fitted time constants τ_r, τ_d from (2.3) in the inset.

The two measurements of the 50 µm thick PET (green) indicate a high level of consistency in both measurement and manufacturing techniques.

5.2 Time constants

To assess the consistency of the estimated parameters for several power density levels, a standard gain horn (MVG SGH2650-42) operating at 28 GHz was positioned 20 mm away from a 204 element metasurface, creating an illumination covering various power levels as depicted in Fig. 9. This figure illustrates the measured power density for each element listed in descending order. The measurement duration was 12 periods, equivalent to 60 s. For lower power densities, it is evident that the signal becomes more susceptible to noise. The rise and decay time constants for each element were then estimated and are depicted in the inset in Fig. 9, where each point represents an element and the color indicates the received power density at that specific point. The estimated values cluster around 0.7 s–0.8 s for both values but become more dispersed as the measured power density decreases, indicating increased susceptibility to noise. However, as shown in Fig. 8, variations in the estimated time constants do not necessarily alter the overall measured signal (temperature difference).

5.3 Sensitivity

The sensitivity during measurements of power density using a 125 µm PET sheets, observing 204 elements corresponding to a surface area of 58 cm^2, is depicted in Fig. 10. In the figure the measured temperature increase, ΔT, of 15 of the observed elements from a measurement of an open-ended waveguide probe positioned 20 mm away, operating at 28 GHz, is displayed. The measurement time was 60 s with the camera operating at 25 Hz. The trend is linear through the region but noise starts to influence lower power density levels. The absolute scale on the y-axis

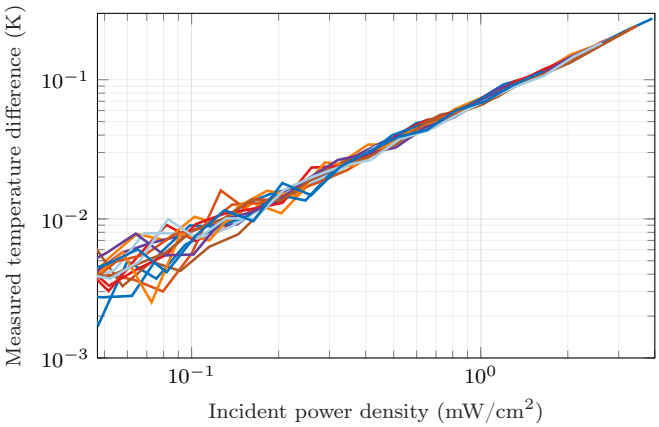

Figure 10: Measured temperature difference for various incident power densities from 15, out of 204, elements in view.

holds less significance, being dependent on the chosen region of interest, Fig. 3 (b). What matters more is the linearity between input power density and observed power density. It is important to note that by employing a region of interest, the temperature increase in units of K can be artificially reduced, potentially falling below the sensitivity of the camera as it is averaged over an area.

6 Antenna measurement results

The technique is now demonstrated for two of the primary use cases, amplitude fault detection and imaging antenna near-field at a specified distance with information on power density. For all measurements, the IR camera, FLIR A655sc, was positioned in a plane parallel to the metasurface at a distance of 20 cm.

6.1 Amplitude fault detection

The measurements of fault detection took place within a semi-anechoic chamber at ReQuTech in Linköping, Sweden. A 16×16 element antenna array was mounted on a stationary turntable. This circularly polarized transmitting (Tx) antenna is designed to operate within the Ka-band frequency range, specifically 27.5 GHz to 31 GHz. The measurements were conducted at a single frequency, 27.6 GHz right-handed circularly polarized, using a signal generator that was linked to the array antenna. A pulse generator was employed to periodically modulate the signal according to (2.2).

An antenna control unit was connected to the array antenna, enabling control of the amplitudes of individual elements. The antenna array elements were individually controlled to create a smiley face pattern. This involved activating 36 out of the 256 antenna array elements, each transmitting equal power, while the rest were deliberately turned off. The metasurface was positioned, and secured using spacers, in close proximity to the array, 3 mm away, as displayed in Fig. 11 (a) and 180

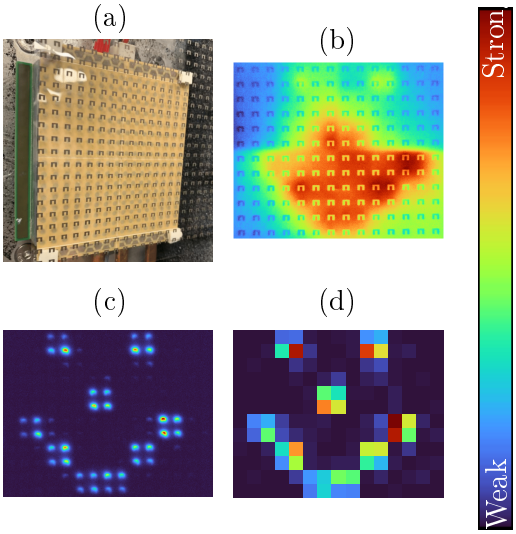

Figure 11: Amplitude fault detection over $52\,\mathrm{cm}^2 \approx 6.5 \times 7\,\lambda^2$ surface of array antenna [28]. (a) image of metasurface over antenna array. (b) Example frame of temperature distribution in the time domain. (c) Frequency content corresponding to a modulation of 0.2 Hz. (d) Processed data displaying active elements and transmitted power. The colorbar phenomenologically indicates strong or weak signal strength.

metasurface elements were tracked. The electronics behind the radiating structure generated heat in certain regions, visible in Fig. 11 (b) in which a raw frame from the IR camera is displayed. However, this was not visible in the 0.2 Hz component of the frequency domain data in (c). In Fig. 11 (c) and the time-domain processed image (d), where each element is treated as a measurement point, we can observe where the antenna is radiating as well as differences between regions of the patch where the output power varied. The measurement was processed in real-time over the displayed surface of $6.5 \times 7\,\lambda^2$ with sufficient information after half a period, 2.5 s. Various amplitude patterns were tested, with the amplitude levels being adjusted. The results showed that changes smaller than 0.5 dB in amplitude could be detected.

The objective was to identify the radiating elements of the transmitting array. The observed variations may stem from differences in transmitting power. However, it is important to note that with the manufactured metasurface and a periodicity different from that of the transmitting array, there may be a slight misalignment towards the edge elements. This, coupled with slight variations in distance to the antenna, could contribute to the observed variations in the measured power densities.

6.2 Near-field imaging

The previously mentioned open-ended waveguide probe, see inset of Fig. 12, was positioned at a distance of $z = 5\,\mathrm{mm}$ from the metasurface with a transmitted

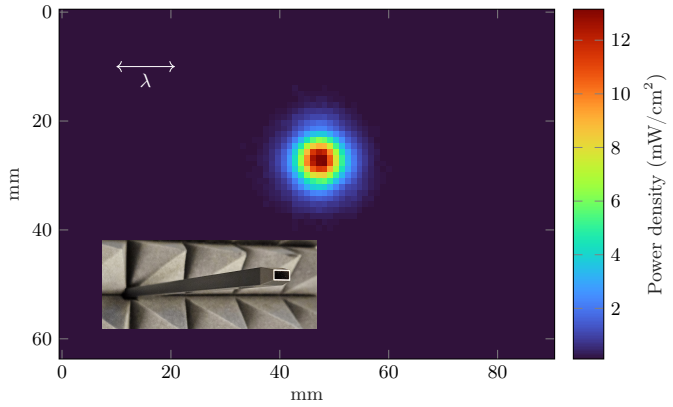

Figure 12: Combined measurement of the power density of an open-ended waveguide probe using 25 metasurface position. The inset image displays the probe.

power of 10 mW (10 dBm) and measured using 204 metasurface elements. Due to the small footprint of the probe in terms of wavelength, the measured image, if displayed as a $\lambda/2$-sampled image similar to Fig. 11(d), appears coarse. To achieve a more densely sampled image of the near field, the metasurface is shifted in the x and y directions, and multiple images are combined to generate a compound image. The co-polarization measurement conducted in this manner is depicted in Fig. 12. The shifts result in a total of 25 measurements of 60 s (5100 measurement points), the shift distance being $\Delta l = \lambda/10 = 1.07$ mm per measurement. As indicated by Fig. 4, similar results are expected for measurements with fewer measured periods. We observe that the field is predominantly localized within a single wavelength. The metasurface measures across various power density levels, resulting in a cohesive representation of the power density with a smooth distribution. Considering this as a known source regarding output power, an extra measurement of cross-polarization was employed to convert the measured temperature difference, ΔT, into power density for all elements on the metasurface.

A comparable method was employed to conduct near-field measurements of a linearly polarized Sony mobile mock-up phone operating at 28 GHz. The phone was assessed in two primary planes located 5 mm away from the nearest point of the phone and connector casing. These planes, along with the phone, are illustrated in Fig. 13. The image reveals four individually fed antennas, with connectors protruding from the chassis. One antenna, highlighted by orange circles, served as the transmitter. As in previous measurements, the phone transmitted a modulated 28 GHz signal with a measured total output power of 32.9 mW (15.2 dBm) and was measured using 204 metasurface elements. To enhance near-field image detail, multiple measurements were taken with varied offsets of the metasurface and subsequently combined. This approach provided a densely sampled depiction of the power density, as showcased in Fig. 12. The metasurface underwent scanning with an incremental step size of $\lambda/10$ in both principal directions, yielding 25 measurements, each lasting 60 s.

In the right column, the measured x-polarized field is depicted for the two planes,

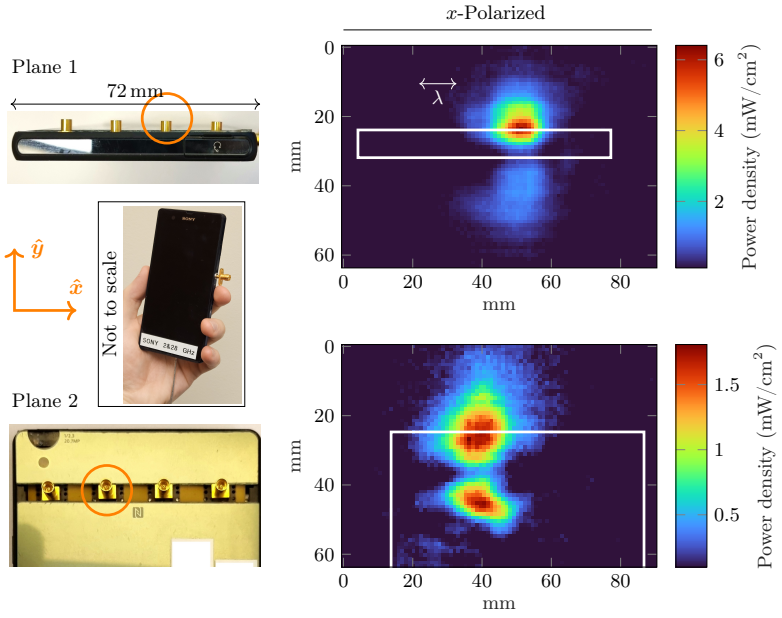

Figure 13: Measured power density for x-polarized electric field of a phone mock-up (left column) at 28 GHz over a $58\,\mathrm{cm}^2 \approx 8 \times 6\,\lambda^2$ area for the two imaged planes (rows). The measured plane was 5 mm away from the device and consist of 25 combined measurements similar to Fig. 12. The transmitting port is highlighted by the orange circles. The white outlines in the measurements display the edge of the phone mock-up chassis.

with a white outline marking the phone mockup case's edge. Analogous to Fig. 12, a smoothly sampled field is presented, revealing higher power density around the radiating element's position, alongside spatial variations on a sub-wavelength scale. Plane 2 exhibits a power density $3-4$ times lower than plane 1. Comparable phone measurements have been conducted in previous studies [20].

7 Conclusion

The measurement technique presented here, which involves heating a metasurface through incident radiation, proves effective in mmWave measurements. It can differentiate between linear polarizations and measure field amplitudes (electric field squared). The measured amplitude represents a cumulative response across the bandwidth of the metasurface elements. Consequently, the ability to resolve individual frequencies is contingent upon the performance of the transmitting device or the associated signal generator.

We have demonstrated how an IR camera capturing images of a metasurface at 27.6 GHz, and 28 GHz, can be used in demonstrating amplitude fault detection in antenna arrays and near-field measurements of a hand-held device. The technique utilizes a modulated input signal, showing promising potential for efficiently conducting incident power density measurements rapidly, in $2.5-60$ seconds, by automated image processing on the IR camera feed. This enables acquiring mmWave measurements over electrically large surfaces in real time.

Unlike previous comparable soldered designs [19], the new approach allows for straightforward manufacturing and is adaptable to various frequencies. Compared to alternative designs, this approach exhibits a lower relative focus of thermal energy. Employing different manufacturing techniques, a resistive element could potentially yield a superior signal response by reducing area and, consequently, mass to enhance the overall signal response.

Data post-processing primarily includes segmenting into elements, potentially applying fast Fourier transforms, and fitting to known functions, all executed in real time without substantially prolonging the measurement duration. Notably, utilizing metasurface elements allows for differential measurements between localized hot and cold regions. This approach efficiently addresses background environments that are challenging to manage with homogeneous structures.

In these measurements, the normalization process to obtain units of $\mathrm{mW/cm^2}$ relies on a priori knowledge of the output power. Future work will explore the use of a known source for individual calibration of elements and address potential interactions and further effects in heat transfer.

Understanding the reflection properties of the metasurface and, subsequently, its connection to the measured device under test is crucial for comprehensive insights. In future research, it is of interest to validate the reflection properties and improve manufacturing control. Further, it is interesting from a near-field interaction perspective to explore any potential influence of the measurement distance in the near-field, along with investigating correction possibilities. While this aspect

may not be the primary focus, it could unlock opportunities for near-to-far-field conversion through the amalgamation of multiple amplitude measurements, a capability inherent in this technique.

The technique presented in this paper is a particularly appealing approach due to its scalability with contemporary manufacturing techniques, offering viable solutions for measurements extending beyond 100 GHz. This scalability ensures its relevance and applicability in addressing the evolving needs and challenges posed by high-frequency measurements.

Acknowledgment

This work was supported by ELLIIT - an Excellence Center at Linköping-Lund in Information Technology.

The authors would like to thank Jan Strandberg at RISE for valuable help with screen printing, Marcus Comstedt, Bogdan Tanasa, and Daniel Kelly-Johansson at ReQuTech for antenna software and hardware preparations before the tests and Zhinong Ying at Sony Mobile for providing the mock-up phone.

References

[1] Y. Aleeva and B. Pignataro. "Recent advances in upscalable wet methods and ink formulations for printed electronics". *J. Mater. Chem. C* 2 (32 2014): pp. 6436–6453.

[2] D. L. Balageas, P. Levesque, and A. A. Deom. "Characterization of electromagnetic fields using a lock-in infrared thermographic system". In: *Thermosense XV: An International Conference on Thermal Sensing and Imaging Diagnostic Applications*. Vol. 1933. International Society for Optics and Photonics. 1993, pp. 274–285.

[3] F. Boccardi, R. W. Heath, A. Lozano, T. L. Marzetta, and P. Popovski. "Five disruptive technology directions for 5G". *IEEE Commun. Mag.* 52 (2) (2014): pp. 74–80.

[4] S Braun. "The synchronous (time domain) average revisited". *Mechanical Systems and Signal Processing* 25 (4) (2011): pp. 1087–1102.

[5] K. Brown. "Far-field antenna pattern measurement using near-field thermal imaging". *IEEE Trans. Antennas Propag.* 66 (3) (2018): pp. 1488–1496.

[6] Y. Chung, S. Lee, and W. Kim. "Latest advances in common signal processing of pulsed thermography for enhanced detectability: a review". *Applied Sciences* 11 (24) (2021).

[7] J.-H. Deng, H. Xiong, Q. Yang, M. Suo, J.-Y. Xie, and H.-Q. Zhang. "Metasurface-based microwave power detector for polarization angle detection". *IEEE Sensors Journal* 23 (19) (2023): pp. 22459–22465.

[8] M. E. Eltayeb, T. Y. Al-Naffouri, and R. W. Heath. "Compressive sensing for millimeter wave antenna array diagnosis". *IEEE Trans. on Communication* 66 (6) (2018): pp. 2708–2721.

[9] K. Fan, J. Y. Suen, X. Liu, and W. J. Padilla. "All-dielectric metasurface absorbers for uncooled terahertz imaging". *Optica* 4 (6) (2017): pp. 601–604.

[10] S. Faure, J.-F. Bobo, D. Prost, F. Issac, and J. Carrey. "Electromagnetic field intensity imaging by thermofluorescence in the visible range". *Phys. Rev. Appl.* 11 (5 2019): p. 054084.

[11] L. G. Gregoris and K. Iizuka. "Thermography in microwave holography". *Applied optics* 14 (7) (1975): pp. 1487–1489.

[12] W. He, B. Xu, L. Scialacqua, Z. Ying, A. Scannavini, L. J. Foged, K. Zhao, C. Di Paola, S. Zhang, and S. He. "Fast power density assessment of 5G mobile handset using equivalent currents method". *IEEE Trans. Antennas Propag.* 69 (10) (2021): pp. 6857–6869.

[13] W. Hong, K.-H. Baek, and S. Ko. "Millimeter-wave 5G antennas for smartphones: overview and experimental demonstration". *IEEE Trans. Antennas Propag.* 65 (12) (2017): pp. 6250–6261.

[14] J. R. Howell, M. P. Menguc, and R. Siegel. "Thermal Radiation Heat Transfer". CRC Press, 2010.

[15] L. Khan, I. Yaqoob, M. Imran, Z. Han, and C. Hong. "6G wireless systems: a vision, architectural elements, and future directions". English. *IEEE Access* 8 (2020): pp. 147029–147044.

[16] S. A. Kuznetsov, A. G. Paulish, M. Navarro-Cía, and A. V. Arzhannikov. "Selective pyroelectric detection of millimetre waves using ultra-thin metasurface absorbers". *Scientific reports* 6 (2016): p. 21079.

[17] S. A. Kuznetsov, A. G. Paulish, A. V. Gelfand, P. A. Lazorskiy, and V. N. Fedorinin. "Bolometric THz-to-IR converter for terahertz imaging". *Applied Physics Letters* 99 (2) (2011): p. 023501.

[18] M. Li, Z. Yuan, Y. Lyu, P. Kyösti, J. Zhang, and W. Fan. "Gigantic MIMO channel characterization: challenges and enabling solutions". *IEEE Communications Magazine* 61 (10) (2023): pp. 140–146.

[19] J. Lundgren, M. Gustafsson, D. Sjöberg, and M. Nilsson. "IR and metasurface based mm-wave camera". *Applied Physics Letters* 118 (18) (2021): p. 184104.

[20] J. Lundgren, J. Helander, M. Gustafsson, D. Sjöberg, B. Xu, and D. Colombi. "A near-field measurement and calibration technique: radio-frequency electromagnetic field exposure assessment of millimeter-wave 5G devices". *IEEE Antennas Propag. Mag.* 63 (3) (2021): pp. 77–88.

[21] M. Maggi, S. Hidri, L. Marnat, M. Ettorre, G. Orozco, M. Margalef-Rovira, C. Gaquière, and K. Haddadi. "Millimeter-wave phased arrays and over-the-air characterization for 5G and beyond: overview on 5G mm-wave phased arrays and OTA characterization". *IEEE Microwave Magazine* 23 (5) (2022): pp. 67–83.

[22] X. Maldague and S. Marinetti. "Pulse phase infrared thermography". *Journal of Applied Physics* 79 (5) (1996): pp. 2694–2698.

[23] G. Medina, A. S. Jida, S. Pulipali, R. Talwar, N. A. J, T. Y. Al-Naffouri, A. Madanayake, and M. E. Eltayeb. "Millimeter-wave antenna array diagnosis with partial channel state information". In: *ICC 2021 - IEEE International Conference on Communications*. 2021, pp. 1–5.

[24] M. D. Migliore. "A compressed sensing approach for array diagnosis from a small set of near-field measurements". *IEEE Trans. Antennas Propag.* 59 (6) (2011): pp. 2127–2133.

[25] K. Muzaffar, L. I. Giri, K. Chatterjee, S. Tuli, and S. Koul. "Fault detection of antenna arrays using infrared thermography". *Infrared Physics & Technology* 71 (2015): pp. 464–468.

[26] J. Norgard and R. Musselman. "Direct infrared measurements of phased array near-field and far-field antenna patterns". *Quantitative InfraRed Thermography Journal* 2 (1) (2005): pp. 113–126.

[27] I. Pušnik and G. Geršak. "Evaluation of the size-of-source effect in thermal imaging cameras". *Sensors* 21 (2) (2021).

[28] ReQuTech. *Phased Arrays – Resa Series*. 2023.

[29] M. R. Somalu, A. Muchtar, W. R. W. Daud, and N. P. Brandon. "Screen-printing inks for the fabrication of solid oxide fuel cell films: a review". *Renewable and Sustainable Energy Reviews* 75 (2017): pp. 426–439.

[30] J. Speight. "Lange's Handbook of Chemistry". 16th ed. McGraw-Hill Education, USA, 2005.

[31] D. Wu and G. Busse. "Lock-in thermography for nondestructive evaluation of materials". *Revue Générale de Thermique* 37 (8) (1998): pp. 693–703.

[32] S. Yoon and H.-K. Kim. "Cost-effective stretchable Ag nanoparticles electrodes fabrication by screen printing for wearable strain sensors". *Surface and Coatings Technology* 384 (2020): p. 125308.

[33] M. Zabihipour, R. Lassnig, J. Strandberg, M. Berggren, S. Fabiano, I. Engquist, and P. Andersson Ersman. "High yield manufacturing of fully screen-printed organic electrochemical transistors". *npj Flexible Electronics* 4 (1) (2020): p. 15.

[34] N. Zavanelli and W.-H. Yeo. "Advances in screen printing of conductive nanomaterials for stretchable electronics". *ACS Omega* 6 (14) (2021): pp. 9344–9351.

[35] S. Zheng, H. Wang, P. Das, Y. Zhang, Y. Cao, J. Ma, S. F. Liu, and Z.-S. Wu. "Multitasking MXene inks enable high-performance printable microelectrochemical energy storage devices for all-flexible self-powered integrated systems". *Advanced Materials* 33 (10) (2021): p. 2005449.